



# CoSe<sub>2</sub> nanoparticles embedded MOF-derived Co-N-C nanoflake arrays as efficient and stable electrocatalyst for hydrogen evolution reaction

Xinqiang Wang<sup>a</sup>, Jiarui He<sup>b,\*</sup>, Bo Yu<sup>a</sup>, Baochen Sun<sup>a</sup>, Dongxu Yang<sup>a</sup>, Xiaojuan Zhang<sup>a</sup>, Qinghua Zhang<sup>c</sup>, Wanli Zhang<sup>a</sup>, Lin Gu<sup>c</sup>, Yuanfu Chen<sup>a,\*</sup>

<sup>a</sup> School of Electronic Science and Engineering, State Key Laboratory of Electronic Thin Films and Integrated Devices, University of Electronic Science and Technology of China, Chengdu, 610054, PR China

<sup>b</sup> Department of Mechanical Engineering, The University of Texas at Austin, Austin, Texas, 78712, USA

<sup>c</sup> Beijing National Laboratory for Condensed Matter Physics, Institute of Physics, Chinese Academy of Sciences, Beijing, 100049, PR China

## ARTICLE INFO

### Keywords:

CoSe<sub>2</sub> nanoparticles

CNC nanoflake

Electrocatalysts

Hydrogen evolution reaction

## ABSTRACT

It is still challenging to develop highly efficient and stable non-noble metal-based electrocatalysts for hydrogen evolution reaction (HER). Herein, CoSe<sub>2</sub> nanoparticles embedded Co-N-doped carbon nanoflake arrays (CS@CNC NAs) are grown on carbon cloth (CC) through a co-precipitation and annealing process. The CS@CNC NAs/CC hybrid electrocatalyst shows superior HER performance with a small Tafel slope of 38 mV dec<sup>-1</sup>, an ultralow overpotential of 84 mV at 10 mA cm<sup>-2</sup> and an excellent long-term stability with nearly no decay even after 72 h. The outstanding HER performance of CS@CNC NAs/CC is mainly attributed to the synergistic effects of CoSe<sub>2</sub> nanoparticles and CNC nanoflake arrays, which can not only provide rich active sites, easy access of electrolyte and diffusion of H<sub>2</sub> bubbles, but also guarantee its high conductivity and structural stability. This work provides a novel strategy for the rational fabrication of highly effective and stable transition metal selenide-based electrocatalysts for HER.

## 1. Introduction

The electrochemical hydrogen evolution reaction (HER) has attracted increasing attention because of its essential role for the sustainable hydrogen (H<sub>2</sub>) production [1]. Although platinum-based materials have been identified to be the most efficient HER electrocatalyst, the high cost and extreme lack greatly limit their practical applications [2–4]. Hence, it is desirable to develop highly efficient and stable non-noble metals-based electrocatalysts for HER.

Recently, various non-noble-metal electrocatalysts, including transition metal sulfides [5–7], phosphides [8], nitrides [9], oxides [10], and selenides [11–14], have been demonstrated as promising electrocatalysts for HER. Among these materials, transition metal selenides (TMSs) such as ReSe<sub>2</sub> [15], PtSe<sub>2</sub> [16], MoSe<sub>2</sub> [17], WSe<sub>2</sub> [18], NiSe<sub>2</sub> [19], CoSe<sub>2</sub> [20], and so on, have received growing attention as efficient electrocatalysts for HER, due to their intrinsically high catalytic property, good stability and low-cost. Nonetheless, their HER electrocatalytic performance and stability cannot fully meet the requirements of commercial applications, which are urgently needed to be further improved. Moreover, it demonstrated that the acidic medium is beneficial for HER process, and thus developing high-efficient and stable

electrocatalysts in acidic condition is a critical challenge [21]. Recently, CoSe<sub>2</sub> have been demonstrated as one of the most efficient electrocatalysts for HER in strong acidic media because of its excellent conductivity and superior catalytic property. However, bulk CoSe<sub>2</sub> always presents inferior HER catalytic kinetics because of the lacking exposed active sites and relatively low conductivity [22–25]. Therefore, various CoSe<sub>2</sub>-based nanostructures including nanowire, nanoneedle, nanosheet, have been employed to expose more active sites, expecting to further improve their catalytic activity [26–28]. Moreover, recent reports indicated that the electrocatalytic activity and stability of CoSe<sub>2</sub> can be enhanced by using carbon nanomaterials (e.g., graphene, carbon nanotube and porous carbon) as supports, due to their high conductivity, good chemical stability and relatively large surface area [24]. In particular, carbon nanomaterials with nitrogen (N)-doping have been demonstrated as promising supporting materials for CoSe<sub>2</sub> nanostructures, due to the N dopants in carbon can provide abundant contact sites for the growth of CoSe<sub>2</sub> nanostructures, thereby leading to rich active sites [20]. More importantly, the co-doping of N and metal dopants in carbon nanomaterials can further improve their electrocatalytic activity due to the highly active metal-N sites can promote the adsorption of hydrated protons to form the intermediate H<sub>ads</sub> and

\* Corresponding authors.

E-mail addresses: [jiarui.he@utexas.edu](mailto:jiarui.he@utexas.edu) (J. He), [yfchen@uestc.edu.cn](mailto:yfchen@uestc.edu.cn) (Y. Chen).

<https://doi.org/10.1016/j.apcatb.2019.117996>

Received 21 April 2019; Received in revised form 3 July 2019; Accepted 22 July 2019

Available online 24 July 2019

0926-3373/ © 2019 Elsevier B.V. All rights reserved.

generation of  $H_2$  gas on the carbon surfaces, benefiting to boost the HER performance [21].

Despite some achievements have been made, most of  $CoSe_2$ /carbon composites are in powder forms, thereby a complex electrode preparation process is involved and the undesired polymeric binders have to be used [4]. Unfortunately, the polymeric binders can block the active sites and are easily peeled off from the electrode under the long-time stability test, which greatly limits their practical application [4]. To solve such issues, direct growth of well-aligned nanoarray architectures (nanowires, nanoneedles and nanoflakes) on current collector, has been considered as one of most efficient approaches to achieve high-performance and stable electrocatalysts [29]. The open framework of the nanoarrays can promote the electrolyte penetration and accelerate the diffusion of  $H_2$  bubbles; and the robust mechanical contact between the nanoarrays and the current collector can prevent the active materials falling off, thus guaranteeing a long-term stability [30]. Therefore, to develop a reasonable nanoarray architecture on the conductive substrate is a powerful way to fabricate the high-performance and stable electrocatalysts for HER.

Herein, we report a facile strategy to synthesize  $CoSe_2$  nanoparticles embedded MOF-derived Co-N-doped carbon nanoflake arrays grown on carbon cloth (CS@CNC NAs/CC). When directly employed as a HER catalyst in acidic solution, the CS@CNC NAs/CC delivers an excellent HER performance with a small Tafel slope of  $38\text{ mV dec}^{-1}$  and a very low overpotential of  $84\text{ mV}$  at current density of  $10\text{ mA cm}^{-2}$ , which is very close to expensive Pt/C catalysts and outperforms most of transition metal-based selenides (Table S1). Furthermore, it shows superior long-term stability, maintaining a stable HER performance up to 72 h. These excellent catalytic performances of CS@CNC NAs/CC are attributed to the synergistic effects of the porous CNC NAs framework and the highly dispersed active  $CoSe_2$  nanoparticles in CS@CNC NAs/CC.

## 2. Experimental section

### 2.1. Synthesis of Co-MOF NAs/CC

Cobalt-based metal-organic-frameworks nanoflake arrays grown on carbon cloth (Co-MOF NAs/CC) were fabricated by a coprecipitation process [31]. The Co-MOF is a Co-containing zeolitic imidazolate framework with a leaf-like morphology (ZIF-L-Co). The chemical formula of the Co-MOF is corresponding to  $Co(mim)_2(Hmim)_{1/2}(H_2O)_{3/2}(C_{10}H_{16}N_5O_{3/2}Co)$ , and the crystal structure of Co-MOF is provided in Fig. S1. In a typical procedure, 1.46 g of 2-methylimidazole and 0.65 g of  $Co(NO_3)_2 \cdot 6H_2O$  were dissolved in 50 mL of deionized water, respectively. Then, the two cups of above solution were quickly mixed with continuous stirring for 10 min. Subsequently, a piece of CC substrate ( $2\text{ cm} \times 5\text{ cm}$ ) was immersed into the mixed solution at room temperature for 3 h. Finally, the obtained Co-MOF NAs/CC precursor was washed by DI water and ethanol and then dried at  $60^\circ\text{C}$  overnight.

### 2.2. Synthesis of CS@CNC NAs/CC

The CS@CNC NAs/CC was converted from Co-MOF NAs/CC precursor through a two-step annealing process. Firstly, a piece of Co-MOF NAs/CC was directly annealed at  $650^\circ\text{C}$  for 2 h in argon atmosphere to obtain Co@CNC NAs/CC. Second, a piece of Co@CNC NAs/CC was further annealed at  $400^\circ\text{C}$  for 2 h in Se vapor under argon atmosphere, with 100 mg of Se powder at the upstream side of a tube furnace. The mass loading of CS@CNC NAs on CC is  $\sim 2.2\text{ mg cm}^{-2}$ .

### 2.3. Synthesis of CNC NAs/CC

The CNC NAs/CC was obtained by an etching process. Typically, a piece of Co@CNC NAs/CC was immersed into 2 M HCl solution for 24 h. Then, the obtained CNC NAs/CC was washed with DI water and ethanol repeatedly and then dried at  $60^\circ\text{C}$  overnight.

### 2.4. Synthesis of CS NAs/CC

A piece of Co-MOF NAs/CC ( $2\text{ cm} \times 5\text{ cm}$ ) was immersed into an ethanol solution containing 200 mg of  $Co(NO_3)_2 \cdot 6H_2O$ . After reaction at  $80^\circ\text{C}$  for 120 min, the Co-MOF NAs/CC were transformed into Co-layered double hydroxide (LDH) on CC (Co-LDH NAs/CC). Then, a piece of Co-LDH NAs/CC was annealed at  $400^\circ\text{C}$  for 2 h in Se vapor under argon atmosphere.

### 2.5. Synthesis of Pt/C/CC

For comparison, 20% Pt/C catalyst modified CC (Pt/C/CC) was prepared as follows. A certain amount of Pt/C catalysts was dispersed in 900  $\mu\text{L}$  of mixed solution (200  $\mu\text{L}$  of ethanol and 700  $\mu\text{L}$  of water), and sonicated for 20 min. Then, 100  $\mu\text{L}$  of Nafion solution was added the mixed solution under sonication to prepare a homogeneous suspension. Finally, the above suspension was uniformly loaded onto the surface of CC and dried at  $60^\circ\text{C}$ . As a result, the mass loading of Pt/C catalysts on CC is  $\sim 10\text{ mg cm}^{-2}$ .

### 2.6. Characterizations

The chemical states and crystalline structures of as-prepared samples were detected by using X-ray photoelectron spectroscopy (XPS, Al  $K\alpha$  radiation) and X-ray diffraction (XRD, Rigaku diffractometer), respectively. The Raman spectra were obtained by using a Raman microscope (532 nm, Horiba). Aberration-corrected HAADF-STEM was performed by JEOL JEM-ARM200CF at 200 kV with double spherical aberration correctors (CEOS GmbH, Heidelberg, Germany) and cold field emission gun. The morphologies of CS@CNC NAs/CC and other samples were imaged by scanning electron microscopy (SEM, JSM 7000 F, JEOL) and transmission electron microscopy (TEM, Tecnai F20, 200 kV).

### 2.7. Measurements of electrocatalytic properties

The HER performances of the samples were investigated in 0.5 M  $N_2$ -saturated  $H_2SO_4$  solution at an electrochemical workstation (CHI660D). A saturated calomel electrode (SCE) and a graphite rod were employed as the reference and counter electrode, respectively. Meanwhile, a piece of CC, CNC NAs/CC, CS NAs/CC, CS@CNC NAs/CC or Pt/C/CC with an area of  $1\text{ cm}^2$  was used as working electrode directly. The line scan voltammograms (LSV) curves were obtained with a scanning rate of  $5\text{ mV s}^{-1}$  from 0.254 to  $-0.346\text{ V}$  (vs RHE). The cyclic voltammetry measurements (CVM) were recorded at different scan rates ( $20\text{--}120\text{ mV s}^{-1}$ ) in the voltage region of 0.1–0.3 V (vs RHE). The AC impedance spectra were carried out at an overpotential of 0.146 V (vs RHE) in the frequency range of 0.1 Hz–100 kHz. The stability of CS@CNC NAs/CC was estimated by the constant voltage chronoamperometry (72 h) and a successive CV test (2000 cycles). In this work, all the potential values were  $iR$ -compensated and calibrated to reversible hydrogen electrodes (RHE,  $E_{RHE} = E_{SCE} + 0.254\text{ V} - iR$ ). The  $H_2$  amount was analyzed by online gas chromatography (GC9790, argon as carrier gas) under constant current densities of  $10\text{ mA cm}^{-2}$  through autosampling every 20 min.

## 3. Results and discussion

As illustrated in Fig. 1,  $CoSe_2$  nanoparticles embedded MOF-derived Co-N-doped carbon nanoflake arrays on carbon cloth (CS@CNC NAs/CC) was successfully converted from cobalt-based metal-organic-frameworks nanoflake arrays grown on carbon cloth (Co-MOF NAs/CC) through a two-step annealing process. Firstly, the Co-MOF NAs/CC was fabricated in room temperature by a solution method according to previous reports [32–34]. Secondly, the Co-MOF NAs/CC was annealed at  $650^\circ\text{C}$  for 2 h in Argon atmosphere. During the annealing process,

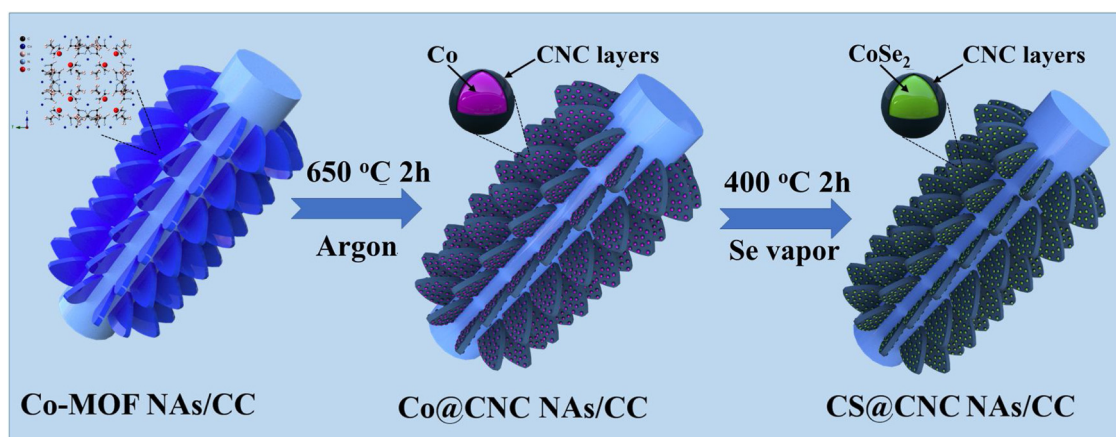


Fig. 1. Schematic illustration of the synthesis procedure of CS@CNC NAs/CC.

the organic ligands and a small number of Co ions were transformed into porous Co-N-doped carbon nanoflake arrays (CNC NAs), and most of Co ions were reduced to Co nanoparticles, thus forming Co@CNC NAs/CC [35]. Thirdly, the Co@CNC NAs/CC was further annealed at 400 °C for 2 h in Se vapor. In this stage, the Co nanoparticles reacted with Se vapor and transformed into CoSe<sub>2</sub> nanoparticles and CNC NAs matrix was well maintained; thus, the CS@CNC NAs/CC can be obtained.

The microstructures of CS@CNC NAs/CC and other control samples

were first characterized by SEM. It can be seen that the Co-MOF NAs grown on CC have a uniform nanoflake arrays (Fig. 2a and b) with an average thickness of 200 nm and smooth surfaces (Fig. 2c). After annealing at 650 °C for 2 h in Ar atmosphere, the nanoflake arrays are well maintained (Fig. 2d) except for some changes on the surfaces of the nanoflakes. The enlarged views show the top edges of the nanoflakes slightly deformed and many Co nanoparticles formed on the nanoflakes (Fig. 2e). Meanwhile the thickness of the nanoflakes shrank to ~ 90 nm in the annealing process (Fig. 2f). As the HAADF-STEM image shown in

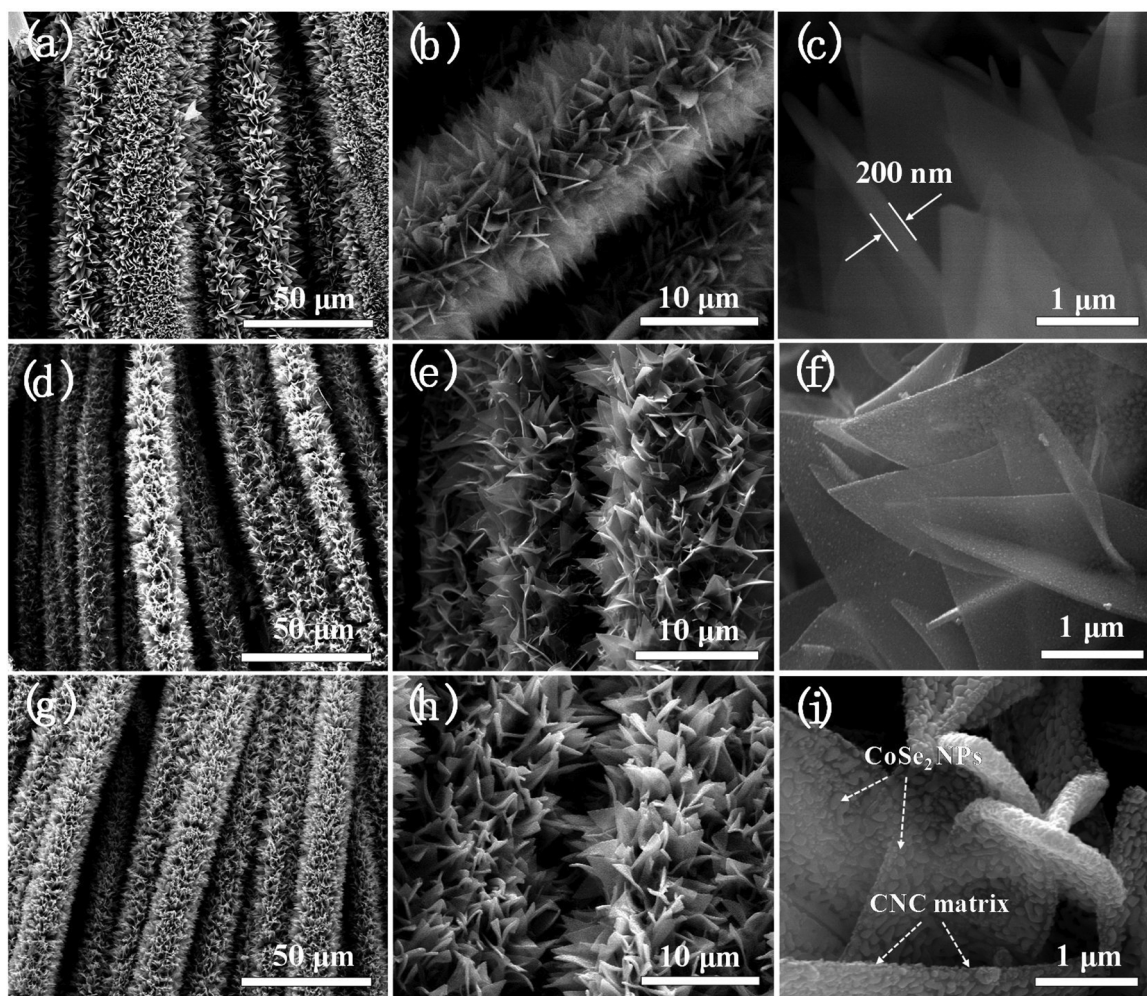
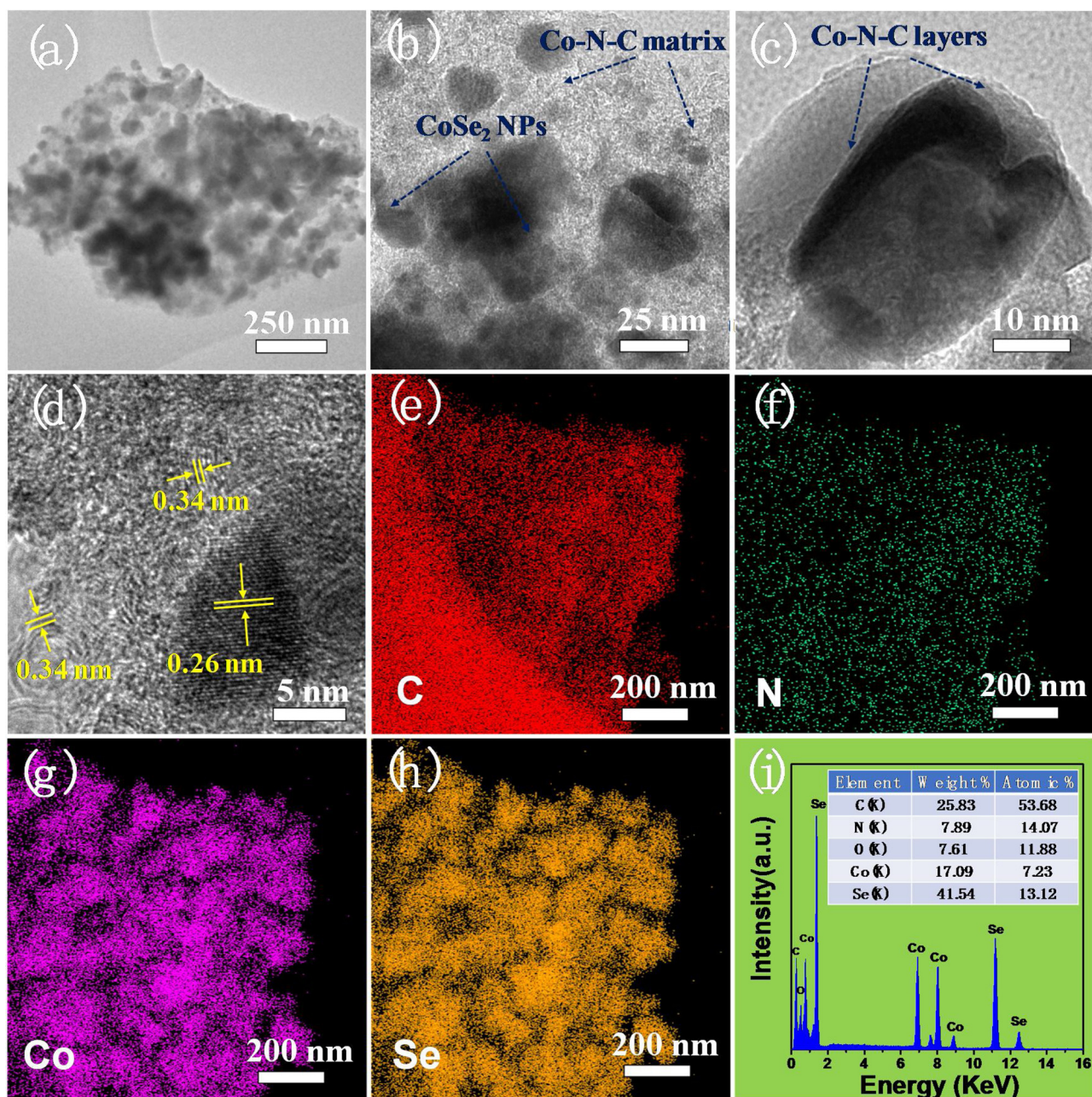


Fig. 2. (a–c) SEM images of Co-MOF NAs/CC. (d–f) SEM images of Co@CNC NAs/CC. (g–i) SEM images of CS@CNC NAs/CC.





**Fig. 3.** (a–c) TEM images of CS@CNC NAs. (d) HRTEM image of CS@CNC NAs. (e–h) EDS elemental mapping images of CS@CNC NAs. (i) EDS spectrum of CS@CNC NAs.

Fig. S2a, one can observe that some Co-aggregation happens during the preparation process. It suggests that most of the Co ions were reduced to Co metal, which is simultaneously aggregated to Co nanoparticles. In addition, a number of atomically dispersed bright spots are apparent in the N-doped carbon support (Fig. S2b), which are ascribed to Co atom sites, indicating the formation of Co-N-C matrix. After selenization process, the CS@CNC NAs/CC perfectly maintains the nanoflake arrays morphologies (Fig. 2g and h). Besides, it shows that the CoSe<sub>2</sub> nanoparticles are uniformly embedded on the surface of CNC NAs matrix (Fig. 2i), which can maximize the exposed reactive sites. Moreover, the open framework can greatly promote the easy access of electrolyte and diffusion of H<sub>2</sub> bubbles [36]. For comparison, the bare CS NAs/CC shows a hierarchical nanoflake morphologies with some aggregation (Fig. S3).

The microstructures of CS@CNC NAs obtained from CC substrate were further examined by TEM at different magnification. As observed

in Fig. 3a, CoSe<sub>2</sub> nanoparticles are uniformly embedded on the surface of CNC nanoflake, which matches well with the SEM results. Fig. 3b further demonstrates the diameters of CoSe<sub>2</sub> nanoparticles on CNC nanoflake matrix are around 10–50 nm. It is worth noted that the CNC nanoflake can not only act as matrix for the uniform dispersion of CoSe<sub>2</sub> nanoparticles, but also provide a rapid channel for electrons transfer [21]. In the enlarged view (Fig. 3c), it can be seen that CoSe<sub>2</sub> nanoparticles on the CNC nanoflake surface are tightly encapsulated within ultrathin carbon layers, which can not only promote the adsorption of hydrated protons to form the intermediate H<sub>ads</sub> on the interfaces and generation of H<sub>2</sub> gas on carbon surfaces, thus benefiting to boost the HER kinetics, but also protect CoSe<sub>2</sub> nanoparticles from external influences, thus enhancing the stability in HER process [37–39]. The HRTEM image (Fig. 3d) reveals that the lattice fringe of 0.26 nm corresponds to the (111) lattice plane of CoSe<sub>2</sub>, and the lattice spacings of 0.34 nm are ascribed to the (002) lattice plane of carbon [24]. The

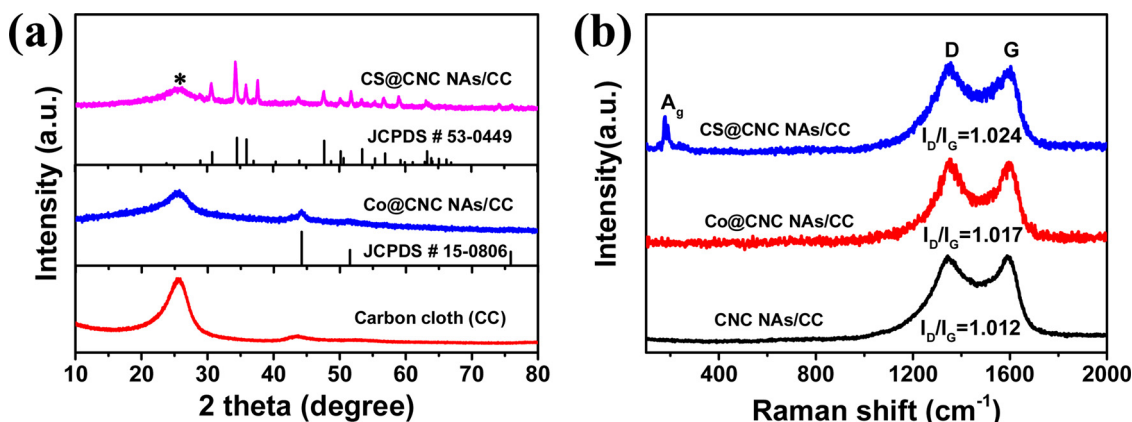


Fig. 4. (a) XRD patterns of bare CC, Co@CNC NAs/CC and CS@CNC NAs/CC. (b) Raman spectra of CNC NAs/CC, Co@CNC NAs/CC and CS@CNC NAs/CC.

typical nanoflake architecture of CS@CNC NAs was further proved by the HAADF-STEM and EDS elemental mappings. As shown in Fig. 3e–h, the elements of Co, Se, C and N are uniformly distributed on the nanoflake (Fig. S4), revealing the uniform dispersion of CoSe<sub>2</sub> nanoparticles on CNC nanoflake matrix. The EDS spectrum (Fig. 3i) further demonstrates that the atomic ratio of Se and Co in CS@CNC NAs is 1.81, which is close to its theoretical value. In addition, it shows a very high N content of 14 at% in CS@CNC NAs, indicating the rich Co-N<sub>x</sub> species in the CNC NAs matrix.

The crystal structures of CC, Co-MOF NAs/CC, Co@CNC NAs/CC and CS@CNC NAs/CC samples were analyzed by XRD measurements. It is noted that the characteristic diffraction peaks of Co-MOF NAs/CC (Fig. S5) disappear after the first annealing process, meanwhile two new peaks (Fig. 4a) appear in the XRD pattern of Co@CNC NAs/CC. The peaks at 51.5° and 44.2° correspond to the (200) and (111) crystal planes of cubic Co metal (JCPDS No.15-0806), which indicates the generation of Co metal nanoparticles in the first annealing process. Besides, the XRD pattern (Fig. 4a) of CS@CNC NAs/CC can be well assigned to orthorhombic (JCPDS No.53-0449) and cubic (JCPDS No.65-3327) CoSe<sub>2</sub> phases, suggesting the formation of CoSe<sub>2</sub> in the selenization process. The distinct diffraction peaks located at 30.78°, 34.52°, 35.96°, 43.96°, 47.72°, 50.23°, 53.48°, 56.95°, 59.27° and 63.29° correspond to the (101), (111), (120), (121), (211), (002), (031), (131), (310) and (122) planes of orthorhombic CoSe<sub>2</sub>, while the two peaks marked with triangle assign to (211) and (311) planes of cubic CoSe<sub>2</sub>. Moreover, the broad peak at around 25° originates from the (002) planes of CC substrate. Fig. 4b shows the Raman spectra of CNC NAs, Co@CNC NAs and CS@CNC NAs samples. The Raman spectra for the three samples shows two similar peaks located at ~1345.4 and ~1587.2 cm<sup>-1</sup>, which are attributed to the D and G bands of CNC NAs matrix, respectively [40]. Importantly, the three samples present relatively high I<sub>D</sub>/I<sub>G</sub> values, indicating that the co-doping of Co and N atoms causes abundant carbon defects in CNC NAs matrix [41]. It is remarkable that the I<sub>D</sub>/I<sub>G</sub> value of CS@CNC NAs (1.024) is very close to that of Co@CNC NAs (1.017), implying the carbon defects maintained well in the selenization process. These carbon defects caused by Co-N-doping can provide rich Co-N<sub>x</sub> active sites to participate in the catalytic reaction, thus remarkably enhancing the HER performance [42].

X-ray photoelectron spectroscopy (XPS) measurement was conducted to elucidate the chemical states of CS@CNC NAs/CC. The presence of C, N, Co and Se (Fig. S6) in CS@CNC NAs/CC is confirmed by the XPS survey spectrum, and their corresponding high-resolution (HR) XPS spectra are presented in Fig. 5. In Fig. 5a, the binding energies appearing at 778.5, 780.6, 781.7, 793.8 and 796.9 eV are ascribed to Co<sup>0</sup> 2p<sub>3/2</sub>, Co<sup>2+</sup> 2p<sub>3/2</sub>, Co-N<sub>x</sub> species, Co<sup>0</sup> 2p<sub>1/2</sub> and Co<sup>2+</sup> 2p<sub>1/2</sub>, respectively [43–45], which confirms the existence of Co-N<sub>x</sub> species in CNC NAs matrix. Besides, the binding energies of 784.1 and 802.2 eV are attributed to the shakeup satellite peaks of Co 2p [11]. In Fig. 5b,

the two peaks at 55.7 and 54.8 eV are ascribed to Se 3d<sub>3/2</sub> and Se 3d<sub>5/2</sub>, respectively, which reveals the existence of Se<sup>2-</sup> in CS@CNC NAs/CC [46]. In addition, the binding energy of 60.3 eV corresponds to the characteristic peak of Co 3p, and the binding energy of 59.2 eV is assigned to the oxide species of Se edges in CoSe<sub>2</sub> nanoparticles [14]. The XPS spectrum (Fig. 5c) of N 1s can be resolved into three bonds corresponding to pyrrolic (400.8 eV), Co-N<sub>x</sub> (399.5 eV) and pyridinic (398.4 eV) [41]. According to previous report, all the three forms of N in CS@CNC NAs/CC can be employed as active sites in the catalytic reaction [41]. In Fig. 5d, the XPS spectrum of C 1s can be fitted to two peaks, which correspond to C–N (286.6 eV) and C–C (284.6 eV) bonds, respectively [47].

The HER activity of CS@CNC NAs/CC was first investigated by using linear sweep voltammetry (LSV) measurement in 0.5 M H<sub>2</sub>SO<sub>4</sub> electrolyte. For comparison, the performances of CC, CNC NAs/CC, CS NAs/CC and Pt/C/CC electrode were also investigated under the same condition. Fig. 6a presents the LSV curves of CC, CNC NAs/CC, CS NAs/CC, CS@CNC NAs/CC and Pt/C/CC. Compared to bare CC with none catalytic activity, the CNC NAs/CC exhibits a preferable HER activity, which is comparable to CS NAs/CC. This result indicates that the co-doping of Co and N dopants can remarkably enhance the HER performance of carbon materials. Impressively, the LSV curve of CS@CNC NAs/CC is greatly close to Pt/C/CC compared with the control samples, indicating its superior HER performance. As shown in Fig. 6c, the CS@CNC NAs/CC shows a dramatically enhanced catalytic performance with a low overpotential of 84 mV at 10 mA cm<sup>-2</sup>, which is lower than that of CS NAs/CC (197 mV) and CNC NAs/CC (213 mV) and very closed to that of Pt/C/CC (35 mV). To investigate the HER mechanism of these samples, the Tafel slopes (Fig. 6b) were extracted from their corresponding LSV curves based on the Tafel equation ( $\eta = a \log j + b$ , where  $a$  is the Tafel slope and  $b$  is a constant). The Tafel slope of CS@CNC NAs/CC (Fig. 6c) is only 38 mV dec<sup>-1</sup>, which is significantly smaller than those of CNC NAs/CC (106 mV dec<sup>-1</sup>), CS NAs/CC (68 mV dec<sup>-1</sup>), confirming its faster kinetics in the HER process. As we all know, the HER process consists of two steps reaction in acid solution. The first step refers to the adsorption of hydrated proton of electrochemistry ( $\text{H}_3\text{O}^+ + \text{e}^- \rightarrow \text{H}_{\text{ads}} + \text{H}_2\text{O}$ , Volmer reaction); the second step is about the desorption of electrochemistry ( $\text{H}_3\text{O}^+ + \text{H}_{\text{ads}} + \text{e}^- \rightarrow \text{H}_2 \uparrow + \text{H}_2\text{O}$ , Heyrovsky reaction) or the desorption of chemistry ( $\text{H}_{\text{ads}} + \text{H}_{\text{ads}} \rightarrow \text{H}_2$ , Tafel reaction). Generally, the Tafel slope of 30, 40 or 120 mV dec<sup>-1</sup> corresponds to Tafel, Heyrovsky or Volmer reaction, respectively. Herein, the CS@CNC NAs/CC shows a Tafel slope of only 38 mV dec<sup>-1</sup>, suggesting it follows the Volmer–Tafel reaction mechanism during the HER process. Particularly, the reaction mechanism is the same as Pt/C catalysts, further indicating the favourable HER kinetics of the CS@CNC NAs/CC electrode during the HER process. Furthermore, the turnover frequency (TOF) of the samples for the active sites was estimated as shown in Fig. S7. The detailed calculation of TOF



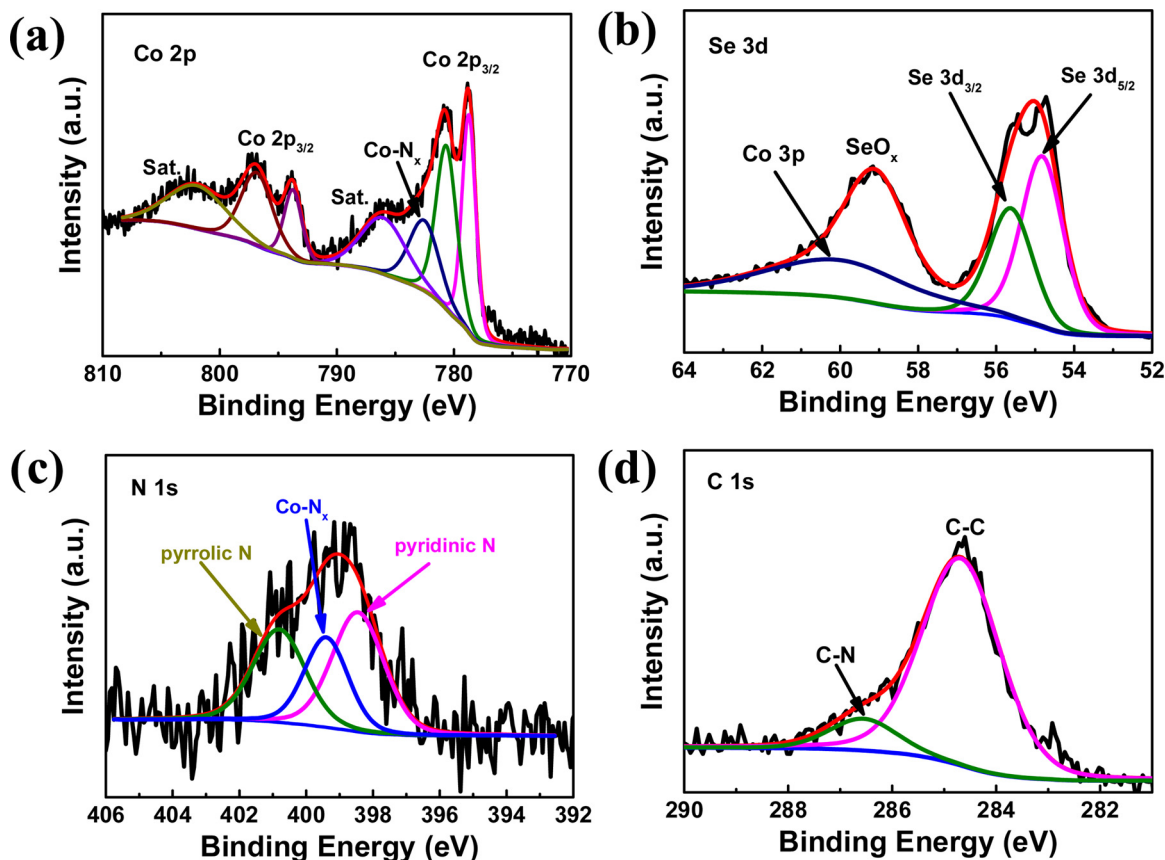


Fig. 5. XPS spectra of CS@CNC NAs/CC: (a) Co 2p, (b) Se 3d, (c) N 1s and (d) C 1s.

is described in the supporting information. The CS@CNC NAs/CC shows a larger TOF of  $15.4 \text{ s}^{-1}$ , compared to those of CS NAs/CC ( $7.7 \text{ s}^{-1}$ ) and CNC NAs/CC ( $1.9 \text{ s}^{-1}$ ) at  $-200 \text{ mV}$  (vs RHE), indicating its high intrinsic activity for HER. In addition, the HER performance of

CS@CNC NAs/CC outperforms most of transition metal-based selenides and other advanced materials (Table S1), rendering it a hopeful substitute for the noble Pt-based catalyst.

The excellent HER performance of CS@CNC NAs/CC is deduced

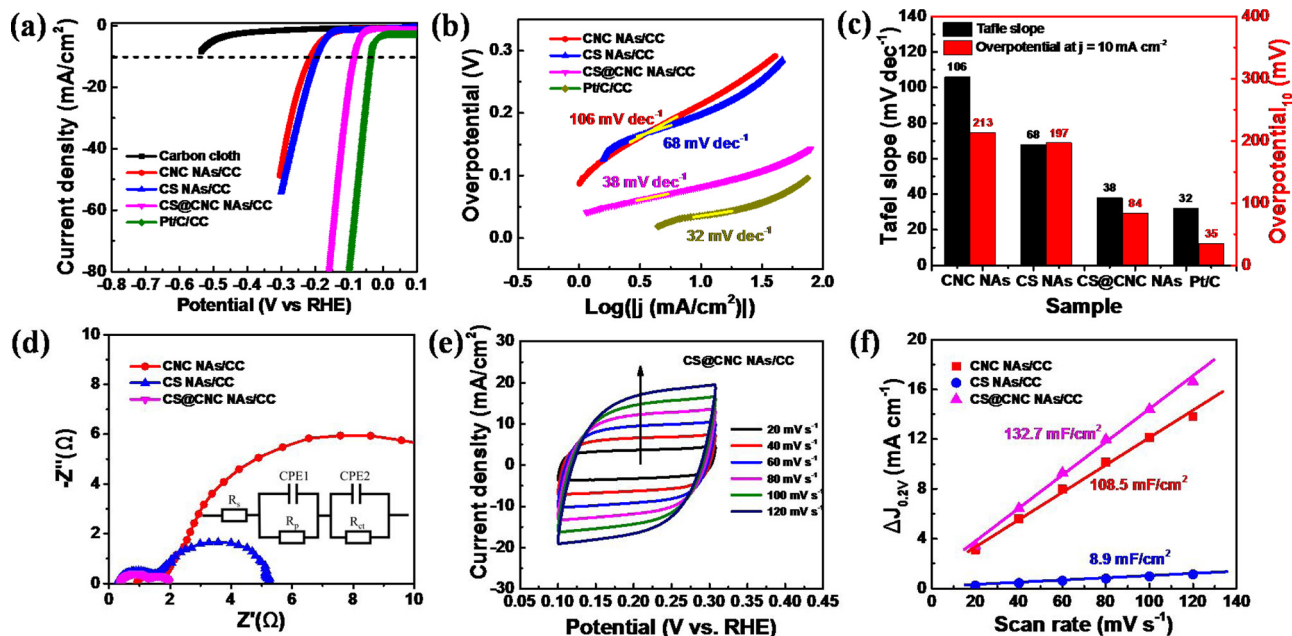


Fig. 6. (a) Polarization curves of CC, CNC NAs/CC, CS NAs/CC, CS@CNC NAs/CC and Pt/C/CC. (b) Corresponding Tafel plots of CNC NAs/CC, CS NAs/CC, CS@CNC NAs/CC and Pt/C/CC. (c) The comparison of HER activity (Tafel slopes and overpotentials at  $10 \text{ mA cm}^{-2}$ ) for CNC NAs/CC, CS NAs/CC, CS@CNC NAs/CC and Pt/C/CC. (d) Nyquist plots of CNC NAs/CC, CS NAs/CC, CS@CNC NAs/CC. (e) Voltammogram of CS@CNC NAs/CC. (f) Estimated  $C_{dl}$  and relative ECSA of CNC NAs/CC, CS NAs/CC, CS@CNC NAs/CC.

benefiting from its open nanoarrays framework, which can not only provide lots of effective channels for the fast electron transfer, but also afford a large electrochemically active surface area (ECSA). To investigate the kinetics on electrode, the Nyquist plots of CNC NAs/CC, CS NAs/CC and CS@CNC NAs/CC were obtained via the AC impedance method. As shown in Fig. 6d, the Nyquist plots for the three samples show two semicircles, which correspond to two time constants in the equivalent circuit (the inset of Fig. 6d). The first semicircle at high-frequency region is related to the porous property of the electrode's surface, and the second semicircle at the relatively low-frequency region corresponds to the interfacial electron transfer resistance ( $R_{ct}$ ), which represents the kinetics of the HER process [48]. After fitting the Nyquist plots, the  $R_{ct}$  value of CS@CNC NAs/CC is identified to be  $1.9 \Omega$ , which is much lower than CNC NAs/CC ( $18.5 \Omega$ ) and CS NAs/CC ( $5.2 \Omega$ ). The lowest  $R_{ct}$  value of CS@CNC NAs/CC indicates its fastest interfacial electron transfer kinetics during the HER process [49]. Generally, the electrochemical double-layer capacitance ( $C_{dl}$ ) can be employed to identify the ECSA. The voltammograms of CNC NAs/CC (Fig. S8a), CS NAs/CC (Fig. S8b) and CS@CNC NAs/CC (Fig. 6e) were performed in the voltage region of 0.1 to 0.3 V (vs RHE) with different scan rates ( $20\text{--}120 \text{ mV s}^{-1}$ ). Based on the CV curves, the plots (Fig. 6f) can be plotted by  $\Delta J/2$  at 0.2 V vs RHE ( $\Delta J = (J_{\text{anodic}} - J_{\text{cathodic}})$ ) versus the scan rate and the linear slope of the plot represents the  $C_{dl}$  value. The  $C_{dl}$  value of CS@CNC NAs/CC is  $132.7 \text{ mF cm}^{-2}$ , which is remarkably larger than those of CNC NAs/CC ( $108.5 \text{ mF cm}^{-2}$ ) and CS NAs/CC ( $8.9 \text{ mF cm}^{-2}$ ), revealing its higher ECSA as well as more active sites for HER. Particularly, the  $C_{dl}$  value of CS@CNC NAs/CC is 15 times as much as CS NAs/CC. This is due to the porous hybrid structure of CS@CNC NAs/CC can adsorb much more hydrated protons to form the intermediate  $H_{\text{ads}}$ .

Besides high catalytic activity, stability in HER process is also a crucial parameter for a practical electrocatalyst. To investigate the stability of CS@CNC NAs/CC in the long-term HER process, a successive CV test (2000 cycles) was performed in the voltage region of  $-0.346 \text{ V} - +0.254 \text{ (vs RHE)}$ . The LSV curve (the inset of Fig. 7a) measured after 2000 CV cycles is well overlapped with initial one, confirming the excellent stability of CS@CNC NAs. As shown in Fig. 7a, the stability of CS@CNC NAs was further investigated under a constant overpotential of  $84 \text{ mV (vs RHE)}$  for 72 h via a chronoamperometry (CA) measurement. The current density ( $10 \text{ mA cm}^{-2}$ ) of CS@CNC NAs/CC presents a slight degradation after the long-term HER process, showing an outstanding stability. The morphology of CS@CNC NAs/CC after stability test have been performed by SEM. As shown in Fig. S9a, even after long-term CA test (72 h), the nanoflake array morphology can be well maintained and the nanoflake arrays cannot be peeled off from CC substrate, revealing the robust contact between the CS@CNC NAs and CC substrate. The high-magnification SEM image (Fig. S9b) further

indicates that the architecture of CS@CNC NAs/CC constructed by  $\text{CoSe}_2$  nanoparticles embedded CNC NAs keeps nearly unchanged, which confirms its excellent structural stability during the long-term HER process. In addition, the CS@CNC NAs/CC after stability test has also been examined by XRD and Raman spectrometer, respectively. Similar to CS@CNC NAs/CC, the XRD pattern after 2000 CV cycles (Fig. S10a) can be well assigned to cubic and orthorhombic  $\text{CoSe}_2$  phases, demonstrating that the  $\text{CoSe}_2$  nanoparticles wrapped by ultrathin CNC layers are very stable in acid media. The Raman characteristic peaks of CS@CNC NAs (Fig. S10b) after 2000 CV cycles are as same as before, which further indicates the excellent stability of  $\text{CoSe}_2$  during the HER process. These results confirm that CS@CNC NAs/CC is a promisingly acid-stable catalyst for HER. Furthermore, to examine the actual rate of  $\text{H}_2$  evolution in the long-term HER process, the Faradaic efficiency (FE) was evaluated by comparing the theoretical value with the experimentally determined  $\text{H}_2$  gas amount [50]. As shown in Fig. 7b, the  $\text{H}_2$  amounts obtained at different reaction durations matches well with the calculated values, indicating the FE is a nearly 100% for the HER.

The electrochemical behaviour of CS@CNC NAs/CC toward HER is illustrated in Fig. S11. The electrons can transfer through the CNC NAs matrix to highly dispersed active CS nanoparticles. Meanwhile, hydronium ions reduced by the transferred electrons at the exposed active sites of CS nanoparticles and Co- $\text{N}_x$  edges are adsorbed on the surface to form the intermediate  $H_{\text{ads}}$ , which are released as hydrogen gas ( $\text{H}_2$ ) at the desorption of chemistry. Considering this investigation, the excellent HER activity of CS@CNC NAs/CC can be explained as follows: (1) The synergetic effects between the highly dispersed active CS nanoparticles and the porous CNC NAs matrix can remarkably enhance the HER performance; the highly dispersed active  $\text{CoSe}_2$  nanoparticles can afford abundant catalytic active sites for HER, and the porous CNC NAs matrix can not only accelerate the access of electrolyte and the diffusion of  $\text{H}_2$  bubbles [21], but also facilitate the faster charge transfer in the HER process [51]. (2) The carbon nanoflake arrays with Co- $\text{N}_x$  doping provide rich Co- $\text{N}_x$  active sites to take part in catalytic reaction, thus benefiting to boost the catalytic activity [52]. (3) The robust contact between CS@CNC NAs and CC substrate guarantees an admirable structural stability in the long-term HER process [53].

#### 4. Conclusions

In this work, a well-defined nanoarray architecture,  $\text{CoSe}_2$  nanoparticles embedded MOF-derived Co-N-doped carbon nanoflake arrays grown on carbon cloth (CS@CNC NAs/CC) has been achieved by using Co-MOFs NAs as a precursor. In the well-designed architecture, the highly active CS nanoparticles encapsulated within ultrathin CNC layers are uniformly distributed on the porous CNC NAs framework. Importantly, the highly dispersed active  $\text{CoSe}_2$  nanoparticles can afford

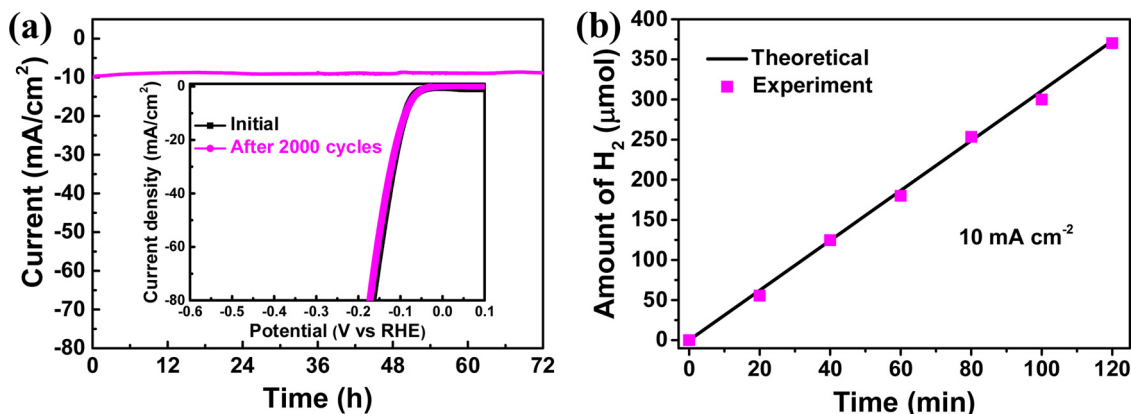


Fig. 7. (a) Time dependence of current density curve of CS@CNC NAs/CC recorded at a potential of  $-84 \text{ mV vs RHE}$ . The inset is stability test of CS@CNC NAs/CC after 2000 CV cycles. (b) Experimentally measured  $\text{H}_2$  production versus theoretically calculated quantities under constant current densities of  $10 \text{ mA cm}^{-2}$ .

abundant catalytic reactive sites, and the porous CNC NAs matrix can accelerate the access of electrolyte and the diffusion of H<sub>2</sub> bubbles. Moreover, the ultrathin CNC layers wrapped on CoSe<sub>2</sub> nanoparticles can not only adsorb much more hydrated protons on their interface to form the intermediate H<sub>ads</sub> and generate H<sub>2</sub> gas on the carbon surfaces, thus benefiting to boost the HER kinetics, but also protect CoSe<sub>2</sub> nanoparticles from external influences, thus enhancing the stability in HER process. When directly employed as a HER catalyst in acidic solution, the CS@CNC NAs/CC delivers an excellent HER performance with a very low overpotential of 84 mV at 10 mA cm<sup>-2</sup> and a small Tafel slope of 38 mV dec<sup>-1</sup>, which outperforms most of transition metal-based selenides and other advanced materials (Table S1). Furthermore, it shows superior long-term stability, maintaining its HER performance up to 72 h. Our work provides a new horizon to rationally synthesize high-efficient and stable transition metal selenides-based hybrid electrocatalysts for HER.

### Declaration of Competing Interest

The authors declare that they have no known competing financial interests or personal relationships that could have appeared to influence the work reported in this paper.

### Acknowledgements

The research was supported by the National Natural Science Foundation of China (Grant Nos. 21773024, 51372033), and National High Technology Research and Development Program of China (Grant No. 2015AA034202).

### Appendix A. Supplementary data

Supplementary data associated with this article can be found, in the online version, at <https://doi.org/10.1016/j.apcatb.2019.117996>.

### References

- [1] S. Anantharaj, S.R. Ede, K. Sakthikumar, K. Karthick, S. Mishra, S. Kundu, *ACS Catal.* 6 (2016) 8069–8097.
- [2] T.A. Shifa, F. Wang, K. Liu, Z. Cheng, K. Xu, Z. Wang, X. Zhan, C. Jiang, J. He, *Small* 13 (2017) 1603706.
- [3] L. Najafi, S. Bellani, R. Oropesa-Nuñez, M. Prato, B. Martín-García, R. Brescia, F. Bonaccorso, *ACS Nano* 13 (2019) 3162–3176.
- [4] Y. Gong, Z. Yang, Y. Lin, J. Wang, H. Pan, Z. Xu, *J. Mater. Chem. A* 6 (2018) 16950–16958.
- [5] Z. Wang, Q. Li, H. Xu, C. Dahl-Petersen, Q. Yang, D. Cheng, D. Cao, F. Besenbacher, J.V. Lauritsen, S. Helveg, M. Dong, *Nano Energy* 49 (2018) 634–643.
- [6] F. Qi, P. Li, Y. Chen, B. Zheng, J. Liu, J. Zhou, J. He, X. Hao, W. Zhang, *Int. J. Hydrogen Energ.* 42 (2017) 7811–7819.
- [7] Y. Zhang, S. Chao, X. Wang, H. Han, Z. Bai, L. Yang, *Electrochim. Acta* 246 (2017) 380–390.
- [8] Y. Lu, W. Hou, D. Yang, Y. Chen, *Electrochim. Acta* 307 (2019) 543–552.
- [9] Y. Zhu, G. Chen, X. Xu, G. Yang, M. Liu, Z. Shao, *ACS Catal.* 7 (2017) 3540–3547.
- [10] P. Li, R. Ma, Y. Zhou, Y. Chen, Z. Zhou, G. Liu, Q. Liu, G. Peng, Z. Liang, J. Wang, *J. Mater. Chem. A* 3 (2015) 15598–15606.
- [11] B. Wang, Z. Wang, X. Wang, B. Zheng, W. Zhang, Y. Chen, *J. Mater. Chem. A* 6 (2018) 12701–12707.
- [12] X. Wang, B. Zheng, B. Wang, H. Wang, B. Sun, J. He, W. Zhang, Y. Chen, *Electrochim. Acta* 299 (2019) 197–205.
- [13] X. Wang, J. He, B. Zheng, W. Zhang, Y. Chen, *Electrochim. Acta* 283 (2018) 1660–1667.
- [14] X. Wang, B. Zheng, B. Yu, B. Wang, W. Hou, W. Zhang, Y. Chen, *J. Mater. Chem. A* 6 (2018) 7842–7850.
- [15] F. Qi, X. Wang, B. Zheng, Y. Chen, B. Yu, J. Zhou, J. He, P. Li, W. Zhang, Y. Li, *Electrochim. Acta* 224 (2017) 593–599.
- [16] Z. Wang, Q. Li, F. Besenbacher, M. Dong, *Adv. Mater.* 28 (2016) 10224–10229.
- [17] B. Zheng, Y. Chen, F. Qi, X. Wang, W. Zhang, Y. Li, X. Li, *2D Mater.* 4 (2017) 25092.
- [18] X. Wang, Y. Chen, B. Zheng, F. Qi, J. He, P. Li, W. Zhang, *Electrochim. Acta* 222 (2016) 1293–1299.
- [19] B. Wang, X. Wang, B. Zheng, B. Yu, F. Qi, W. Zhang, Y. Li, Y. Chen, *Electrochim. Commun.* 83 (2017) 51–55.
- [20] H. Wang, X. Wang, D. Yang, B. Zheng, Y. Chen, *J. Power Sources* 400 (2018) 232–241.
- [21] T. Sun, J. Dong, Y. Huang, W. Ran, J. Chen, L. Xu, *J. Mater. Chem. A* 6 (2018) 12751–12758.
- [22] H. Yue, B. Yu, F. Qi, J. Zhou, X. Wang, B. Zheng, W. Zhang, Y. Li, Y. Chen, *Electrochim. Acta* 253 (2017) 200–207.
- [23] W. Hou, B. Yu, F. Qi, X. Wang, B. Zheng, W. Zhang, Y. Li, Y. Chen, *Electrochim. Acta* 255 (2017) 248–255.
- [24] K. Zhou, J. He, X. Wang, J. Lin, Y. Jing, W. Zhang, Y. Chen, *Electrochim. Acta* 231 (2017) 626–631.
- [25] H. Zhang, B. Yang, X. Wu, Z. Li, L. Lei, X. Zhang, *ACS Appl. Mater. Inter.* 7 (2015) 1772–1779.
- [26] K. Wang, D. Xi, C. Zhou, Z. Shi, H. Xia, G. Liu, G. Qiao, *J. Mater. Chem. A* 3 (2015) 9415–9420.
- [27] C.H. Mu, H.X. Qi, Y.Q. Song, Z.P. Liu, L.X. Ji, J.G. Deng, Y.B. Liao, F. Scarpa, *RSC Adv.* 6 (2016) 23–30.
- [28] W. Zhou, J. Lu, K. Zhou, L. Yang, Y. Ke, Z. Tang, S. Chen, *Nano Energy* 28 (2016) 143–150.
- [29] Y.H. Deng, C. Ye, B.X. Tao, G. Chen, Q. Zhang, H.Q. Luo, N.B. Li, *J. Power Sources* 397 (2018) 44–51.
- [30] W. Wang, L. Yang, F. Qu, Z. Liu, G. Du, A.M. Asiri, Y. Yao, L. Chen, X. Sun, *J. Mater. Chem. A* 5 (2017) 16585–16589.
- [31] J. Zhang, T. Zhang, D. Yu, K. Xiao, Y. Hong, *Crystengcomm* 17 (2015) 8212–8215.
- [32] Y. Li, H. Wang, Y. Li, Q. Wang, D. Li, R. Wang, B. He, Y. Gong, *J. Catal.* 364 (2018) 48–56.
- [33] J. He, Y. Chen, A. Manthiram, *iScience* 4 (2018) 36–43.
- [34] J. He, Y. Chen, A. Manthiram, *Energ. Environ. Sci.* 11 (2018) 2560–2568.
- [35] D. Ji, S. Peng, L. Fan, L. Li, X. Qin, S. Ramakrishna, *J. Mater. Chem. A* 5 (2017) 23898–23908.
- [36] J. Hu, Y. Ou, Y. Li, D. Gao, Y. Zhang, P. Xiao, *ACS Sustain. Chem. Eng.* 6 (2018) 11724–11733.
- [37] S. Peng, L. Li, J. Zhang, T.L. Tan, T. Zhang, D. Ji, X. Han, F. Cheng, S. Ramakrishna, *J. Mater. Chem. A* 5 (2017) 23361–23368.
- [38] Z. Chen, R. Wu, Y. Liu, Y. Ha, Y. Guo, D. Sun, M. Liu, F. Fang, *Adv. Mater.* 30 (2018) 1802011.
- [39] Q. Mo, W. Zhang, L. He, X. Yu, Q. Gao, *Appl. Catal. B: Environ.* 244 (2019) 620–627.
- [40] Y. Liu, Y. Fang, Z. Zhao, C. Yuan, X.W.D. Lou, *Adv. Energy Mater.* 9 (2019) 1803052.
- [41] Y.J. Sa, S.O. Park, G.Y. Jung, T.J. Shin, H.Y. Jeong, S.K. Kwak, S.H. Joo, *ACS Catal.* 9 (2019) 83–97.
- [42] Y. Tong, X. Yu, H. Wang, B. Yao, C. Li, G. Shi, *ACS Catal.* 8 (2018) 4637–4644.
- [43] Y. He, S. Hwang, D.A. Cullen, M.A. Uddin, L. Langhorst, B. Li, S. Karakalos, A.J. Kropf, E.C. Wegener, J. Sokolowski, M. Chen, D. Myers, D. Su, K.L. More, G. Wang, S. Litster, G. Wu, *Energ. Environ. Sci.* 12 (2019) 250–260.
- [44] I. Chiu, C. Li, C. Lee, P. Chen, Y. Tseng, R. Vittal, K. Ho, *Nano Energy* 22 (2016) 594–606.
- [45] W. Liu, M. Shao, W. Zhou, B. Yuan, C. Gao, H. Li, X. Xu, H. Chu, Y. Fan, W. Zhang, S. Li, J. Hui, D. Fan, F. Huo, *ACS Appl. Mater. Inter.* 10 (2018) 38845–38852.
- [46] X. Wang, Y. Chen, B. Zheng, F. Qi, J. He, Q. Li, P. Li, W. Zhang, *J. Alloys. Compd.* 691 (2017) 698–704.
- [47] Y. Xu, W. Tu, B. Zhang, S. Yin, Y. Huang, M. Kraft, R. Xu, *Adv. Mater.* 29 (2017) 1605957.
- [48] X. Wang, H. Zhou, D. Zhang, M. Pi, J. Feng, S. Chen, *J. Power Sources* 387 (2018) 1–8.
- [49] J. Chi, Y. Chai, X. Shang, B. Dong, C. Liu, W. Zhang, Z. Jin, *J. Mater. Chem. A* 6 (2018) 24783–24792.
- [50] M. Zang, N. Xu, G. Cao, Z. Chen, J. Cui, L. Gan, H. Dai, X. Yang, P. Wang, *ACS Catal.* 8 (2018) 5062–5069.
- [51] L. Zeng, K. Sun, X. Wang, Y. Liu, Y. Pan, Z. Liu, D. Cao, Y. Song, S. Liu, C. Liu, *Nano Energy* 51 (2018) 26–36.
- [52] T. Sun, S. Zhang, L. Xu, D. Wang, Y. Li, *Chem. Commun. (Camb.)* 54 (2018) 12101–12104.
- [53] A. Wang, J. Lin, H. Xu, Y. Tong, G. Li, *J. Mater. Chem. A* 4 (2016) 16992–16999.